

Marginal stability boundaries for infinite- n ballooning modes in a quasiaxisymmetric stellarator

S. R. Hudson

Princeton Plasma Physics Laboratory, P.O. Box 451, Princeton, New Jersey 08543

C. C. Hegna

Department of Physics, University of Wisconsin, Madison, Madison, Wisconsin 53706

(Received 30 June 2003; accepted 4 September 2003)

A method for computing the ideal magnetohydrodynamic (MHD) stability boundaries in three-dimensional equilibria is employed. Following Hegna and Nakajima [Phys. Plasmas **5**, 1336 (1998)], a two-dimensional family of equilibria is constructed by perturbing the pressure and rotational-transform profiles in the vicinity of a flux surface for a given stellarator equilibrium. The perturbations are constrained to preserve the MHD equilibrium condition. For each perturbed equilibrium, the infinite- n ballooning stability is calculated. Marginal stability diagrams are thus constructed that are analogous to (s, α) diagrams for axisymmetric configurations. A quasiaxisymmetric stellarator is considered. Calculations of stability boundaries generally show regions of instability can occur for either sign of the average magnetic shear. Additionally, regions of second-stability are present. © 2003 American Institute of Physics. [DOI: 10.1063/1.1622669]

I. INTRODUCTION

A principle aim of stellarator research is to understand the physical mechanisms that limit the plasma stored energy. The expectation is that pressure driven instabilities will be excited as the plasma energy increases relative to the magnetic energy. Since one of the advantages of stellarators is the avoidance of current limiting instabilities, pressure driven instabilities may be critical in limiting stellarator operation.

In theoretical studies of particular configurations, local criterion deduced from ideal magnetohydrodynamic (MHD) ballooning theory are often used to predict the plasma pressure limits of stellarators. There is, however, experimental evidence^{1,2} suggesting that localized ballooning instabilities set a pressure limit that is too pessimistic for stellarators.

The intent of this article is to contribute to the understanding of the physics describing the onset of ideal MHD ballooning instabilities in stellarator configurations. In an effort to understand the physical mechanism that causes ballooning instability, Greene and Chance³ introduced a technique for constructing ballooning stability boundaries. In this method, for a given numerically computed axisymmetric equilibrium, a two-dimensional family of equilibria is constructed by self-consistently imposing perturbations on the pressure gradient and the shear at a given flux surface. This method allows the pressure gradient and average magnetic shear to be varied independently of geometry. For each such constructed equilibrium, the ballooning stability may be examined.

This technique clarified the onset of “second-stability” in tokamak configurations. It was noted that ballooning instabilities arise in regions of unfavorable curvature and small local shear. As the pressure gradient is increased, the increased parallel currents alter the local shear and the zeros of

local shear migrate poloidally. Second-stability is observed when the zeros of the local shear coincide with favorable curvature, and when in the unfavorable curvature regions, the magnitude of the local shear is sufficient to stabilize the ballooning modes.

To what extent these ideas are applicable to the nonaxisymmetric stellarator devices is an area of present research. Stellarator geometry can be far more complicated than that of the tokamak. It has been suggested that second-stability may be difficult to obtain in quasihelical equilibria,⁴ but second-stability has been observed in a quasipoloidal equilibrium.⁵ The existence of a second stable region in stellarators suggests the possibility of high β operation and is an enticing prospect.

A feature related to second stability, which we call “self-stabilization” after Ref. 6 has been observed in various stellarator experiments.^{7–10} In these results, geometrical deformations associated with the Shafranov shift result in configurations which are stable with respect to Mercier modes as pressure is increased. In this article, we use the term second stability to refer to the stabilization of ballooning modes due to pressure induced variations in the local shear, with no geometrical deformations.

Hegna and Nakajima¹¹ extended the theory of Greene and Chance to three-dimensional configurations. In this work, we study the ideal ballooning stability of a family of quasiaxisymmetric stellarator equilibria and present marginal stability diagrams. We find that for this configuration, the existence of second-stability is observed on some magnetic surfaces. While the conventional explanation of the appearance of second-stability (instability ensues when regions of unfavorable curvature overlap regions of small local shear; second-stability occurs through pressure modulations of the local shear) seems plausible, the nonaxisymmetry of stellarators results in a more complicated structure of both the cur-

vature and the local shear and the mechanism of second-stability is less easily demonstrated.

The outline of this paper is as follows. In Sec. II, the theory of the profile variation method is described. The numerical implementation is discussed in Sec. III, and in Sec. IV benchmarking results for an axisymmetric case are presented. The axisymmetric case is useful for developing intuition about the role of curvature and local shear. Section V will present marginal stability diagrams and analysis of a quasisymmetric stellarator. Some similar features of the marginal stability diagrams are observed. The existence of unstable regions for either sign of averaged magnetic shear and the existence of second-stability is observed. Section VI will discuss the effect of field line variation on the stability diagrams. Some discussion of the physical mechanism of ballooning stability, and the characteristics leading to second-stability will be mentioned is given in Sec. VII; however, a full quantitative description of the onset of second-stability is an involved topic and requires further detailed analysis which is left to future work.

II. THEORY

This work is essentially a numerical implementation of the theory presented by Hegna and Nakajima,¹¹ who generalized the work of Greene and Chance.³ By applying variations to, in this case, the pressure gradient and the average magnetic shear at a selected surface of a given equilibrium, and requiring that the coordinate response to the variations be such that the resultant state is also an equilibrium, a two-dimensional family of perturbed equilibria are constructed. Using this method, the effect on ballooning stability of changes in the pressure gradient and changes in the shear may be separately studied, with the surface geometry held fixed. The following shall outline the principles of the method and the key assumptions. For additional details the reader should consult Ref. 11.

The analysis proceeds using Boozer coordinates¹² with (ψ, θ, ζ) being the radial (toroidal flux), poloidal and toroidal coordinates. The magnetic field is written in contravariant and covariant form as

$$\mathbf{B} = \nabla\psi \times \nabla\theta + \iota(\psi) \nabla\zeta \times \nabla\psi, \quad (1)$$

$$\mathbf{B} = \beta(\psi, \theta, \zeta) \nabla\psi + I(\psi) \nabla\theta + G(\psi) \nabla\zeta, \quad (2)$$

where ι is the rotational-transform, G is the poloidal current exterior to ψ , I is the toroidal current interior to ψ , and β is related to the Pfirsch–Schlüter current.

The magnetic field is defined implicitly through the coordinate transform $\mathbf{x}(\psi, \theta, \zeta)$ from Boozer coordinates to Cartesian coordinates. The metric elements of the transformation $g_{ij} = \mathbf{e}_i \cdot \mathbf{e}_j$ are defined by the basis vectors $\mathbf{e}_\psi = \partial_\psi \mathbf{x}$, $\mathbf{e}_\theta = \partial_\theta \mathbf{x}$, and $\mathbf{e}_\zeta = \partial_\zeta \mathbf{x}$. The magnetic field may be written in terms of the basis vectors as

$$\mathbf{B} = (\iota \mathbf{e}_\theta + \mathbf{e}_\zeta) / \sqrt{g}. \quad (3)$$

As Eqs. (1) and (2) represent the same magnetic field the following conditions must be satisfied:

$$\sqrt{g} = (G + \iota I) / B^2, \quad (4)$$

$$G = (g_{\zeta\zeta} + \iota g_{\theta\zeta}) / \sqrt{g}, \quad (5)$$

$$I = (g_{\theta\zeta} + \iota g_{\theta\theta}) / \sqrt{g}, \quad (6)$$

$$\beta = (g_{\psi\zeta} + \iota g_{\psi\theta}) / \sqrt{g}. \quad (7)$$

These equations, and the force balance equation

$$\nabla p = \mathbf{J} \times \mathbf{B}, \quad (8)$$

will be used to derive relationships between the perturbed quantities.

The method of profile variations is to vary the pressure gradient p' and shear ι' at a given surface ψ_b while keeping the pressure p and rotational-transform ι undisturbed (to lowest order). To achieve this, the variable y is introduced:

$$y = \frac{\psi - \psi_b}{\mu}, \quad (9)$$

where $\mu \ll 1$ is a small expansion parameter. By expressing the perturbed quantities as functions of y rather than ψ , derivatives with respect to ψ will introduce a factor μ^{-1} , thus ensuring that the variations in the gradients p' , ι' are lower order than the variations in the pressure and rotational-transform p , ι .

The pressure and rotational-transform profiles are described in the vicinity of a magnetic surface ψ_b by the expansion

$$p(\psi) = p^{(0)}(\psi) + \mu p^{(1)}(y) + \dots, \quad (10)$$

$$\iota(\psi) = \iota^{(0)}(\psi) + \mu \iota^{(1)}(y) + \dots, \quad (11)$$

where $p^{(0)}$, $\iota^{(0)}$ are the pressure and rotational-transform profiles of the undisturbed equilibrium and $p^{(1)}$, $\iota^{(1)}$ are the perturbation profiles (similar notation is used below).

For the perturbed state to satisfy the equilibrium conditions, it is necessary that the magnetic field also be perturbed. This is achieved by perturbing the coordinate transformation

$$\mathbf{x}(\psi, \theta, \zeta) = \mathbf{x}^{(0)}(\psi, \theta, \zeta) + \mu \mathbf{x}^{(1)}(y, \theta, \zeta) + \dots. \quad (12)$$

From this representation, the perturbed basis vectors are determined:

$$\mathbf{e}_\psi = \mathbf{e}_\psi^{(0)} + \partial_y \mathbf{x}^{(1)} + \dots, \quad (13)$$

$$\mathbf{e}_\theta = \mathbf{e}_\theta^{(0)} + \mu \partial_\theta \mathbf{x}^{(1)} + \dots, \quad (14)$$

$$\mathbf{e}_\zeta = \mathbf{e}_\zeta^{(0)} + \mu \partial_\zeta \mathbf{x}^{(1)} + \dots. \quad (15)$$

The basis vectors \mathbf{e}_θ and \mathbf{e}_ζ are undisturbed to lowest order, but the \mathbf{e}_ψ basis vector has order unity variations. It follows that the metric elements $g_{\theta\theta}$, $g_{\theta\zeta}$, and $g_{\zeta\zeta}$ are undisturbed, but that $g_{\psi\psi}$, $g_{\psi\theta}$, and $g_{\psi\zeta}$ have order unity variations. For consistency, both G and I are perturbed similarly to p and ι , but β requires order unity variations as it contains the $g_{\psi\zeta}$ and $g_{\psi\theta}$ metric elements.

As can be seen from the perturbed basis vectors, the key quantity in the coordinate variation is $\partial_y \mathbf{x}^{(1)}$. This is expanded in a basis

$$\frac{\partial \mathbf{x}^{(1)}}{\partial y} = C \mathbf{B} + D \frac{\mathbf{B} \times \nabla \psi}{B^2} + M \frac{\nabla \psi}{g^{\psi\psi}}, \quad (16)$$

where C , D , and M are to be determined. The condition that the magnetic field strength be undisturbed to lowest order is imposed. This is equivalent to requiring that the variation in the Jacobian be zero which, given the perturbed basis vectors, becomes

$$\frac{\partial \mathbf{x}^{(1)}}{\partial y} \cdot \frac{\partial \mathbf{x}^{(0)}}{\partial \theta} \times \frac{\partial \mathbf{x}^{(0)}}{\partial \zeta} = \frac{\partial \mathbf{x}^{(1)}}{\partial y} \cdot \nabla \psi \sqrt{g} = 0, \quad (17)$$

giving the constraint $M=0$. This ensures that the variation $\partial_y \mathbf{x}^{(1)}$ lies within the flux surface. The quantity C may be written $C = \beta^{(1)}/B^2$ due to Eq. (7) and a relation for $\beta^{(1)}$ is obtained from the momentum balance equation.

To obtain an expression for the quantity D the constraints imposed by requiring the perturbations satisfy Eqs. (5), (6) and force balance are utilized. This results in an equation for D ,

$$\begin{aligned} \left(\frac{\partial}{\partial \zeta} + \epsilon \frac{\partial}{\partial \theta} \right) D = & \epsilon^{(1)'} \frac{1}{\oint 1/g^{\psi\psi}} \left(\frac{1}{g^{\psi\psi}} - \oint \frac{1}{g^{\psi\psi}} \right) \\ & - p^{(1)'} \frac{V'(G + \epsilon I)}{\oint 1/g^{\psi\psi}} \left(\frac{\lambda}{g^{\psi\psi}} \oint \frac{1}{g^{\psi\psi}} \right. \\ & \left. - \frac{1}{g^{\psi\psi}} \oint \frac{\lambda}{g^{\psi\psi}} \right), \end{aligned} \quad (18)$$

where

$$\oint Q \equiv \oint \frac{d\theta}{2\pi} \oint \frac{d\zeta}{2\pi} Q \quad (19)$$

is the flux surface average.

All the necessary information to solve for infinite- n ballooning mode equation in the perturbed equilibrium is now obtained. The ballooning equation (28) depends on the following quantities: B^2 and \sqrt{g} , which are required to be undisturbed to lowest order; $g^{\psi\psi}$, which is equivalent to $(g_{\theta\theta}g_{\zeta\zeta} - g_{\theta\zeta}g_{\zeta\theta})/\sqrt{g}^2$ and is undisturbed to lowest order; G , ϵ , and I , which are undisturbed to lowest order; and the normal and geodesic curvatures κ_n , κ_g , and the local shear. The curvatures are defined in Ref. 11:

$$\kappa_n = \frac{(\mathbf{b} \cdot \nabla) \mathbf{b} \cdot \nabla \psi}{g^{\psi\psi}}, \quad (20)$$

$$\kappa_g = \frac{(\mathbf{b} \cdot \nabla) \mathbf{b} \cdot \mathbf{B} \times \nabla \psi}{B^2}. \quad (21)$$

The unit vector in the direction of the magnetic field \mathbf{b} is

$$\mathbf{b} = \frac{\epsilon \mathbf{e}_\theta + \mathbf{e}_\zeta}{|\epsilon \mathbf{e}_\theta + \mathbf{e}_\zeta|}, \quad (22)$$

and $\nabla \psi$ may be written

$$\nabla \psi = \frac{\mathbf{e}_\theta \times \mathbf{e}_\zeta}{\sqrt{g}}. \quad (23)$$

Both these quantities (and \mathbf{B}, B^2) are undisturbed to lowest order; thus, the normal and geodesic curvatures are also undisturbed as no radial derivatives are involved. The local shear used by Ref. 11 is

$$s = \sqrt{g} \frac{\mathbf{B} \times \nabla \psi}{g^{\psi\psi}} \cdot \nabla \times \frac{\mathbf{B} \times \nabla \psi}{g^{\psi\psi}}. \quad (24)$$

This term is disturbed by the perturbations as a radial derivative is involved. Using the contravariant form of \mathbf{B} given in Eq. (1), the local shear is written $s = \epsilon' + \tilde{s}$ where \tilde{s} is given

$$\tilde{s} = \left(\epsilon \frac{\partial}{\partial \theta} + \frac{\partial}{\partial \zeta} \right) \left(\frac{G g_{\psi\theta} - I g_{\psi\zeta}}{\sqrt{g} g^{\psi\psi}} \right). \quad (25)$$

The perturbed part of this is

$$(G \partial_y \mathbf{x}^{(1)} \cdot \mathbf{e}_\theta - I \partial_y \mathbf{x}^{(1)} \cdot \mathbf{e}_\zeta) / (\sqrt{g} g^{\psi\psi}) = D. \quad (26)$$

The term D thus represents how the profile variations affect the local shear. Remarkably, as far as the infinite- n ballooning equation (28) is concerned, it is *only* the local shear that is affected by the profile variations (other than of course p', ϵ'). We conclude that any change in the ballooning stability caused by the profile variations must be due to variations in the local shear.

The ballooning mode equation in the perturbed equilibrium is written by transforming the angle variables $\alpha = \theta - \epsilon \zeta$, $\eta = \zeta$ so that α labels the field line, η labels position along the field line and the $\mathbf{B} \cdot \nabla$ operator becomes

$$\mathbf{B} \cdot \nabla = \frac{1}{\sqrt{g}} \frac{\partial}{\partial \eta}, \quad (27)$$

where $\partial_\eta = \partial_\zeta + \epsilon \partial_\theta$. The ballooning equation is given in a form that highlights the role of the (integrated) local shear,

$$\begin{aligned} \frac{\partial}{\partial \eta} \left(\frac{B^2}{g^{\psi\psi}} + g^{\psi\psi} L^2 \right) \frac{\partial \xi}{\partial \eta} + 2(p^{(0)'} + p^{(1)'}) \sqrt{g} (G + \epsilon I) \\ \times (\kappa_n + \kappa_g L) \xi = \omega^2(\psi, \alpha, \eta_k) \left(\frac{B^2}{g^{\psi\psi}} + g^{\psi\psi} L^2 \right) \xi, \end{aligned} \quad (28)$$

where L is the integrated local shear

$$L = \int_{\eta_k}^{\eta} d\eta' s(\eta'), \quad (29)$$

η_k is the ballooning angle and ω^2 is the ballooning eigenvalue which in general depends on the surface, field line and ballooning angle η_k . This is an ordinary differential equation with boundary condition $\xi(\pm\infty) = 0$. For numerical work, the boundary condition is that $\xi(\pm\eta_\infty) = 0$, where η_∞ is chosen to sufficiently large to contain the mode.

The equilibrium variations describe the separate effects that the variation in p' and ϵ' have on the local shear, and thus on ballooning stability. Taking p' and ϵ' as independent variables, a two-dimensional family of equilibrium surfaces may be constructed. For each surface ballooning stability may be determined and marginal stability curves constructed. Note that if the analysis of the perturbed equilibrium is local to the original surface ψ_b in Eq. (9), as infinite- n ballooning analysis indeed is, then the equations describing how the variations affect the local shear are exact. Variations of any magnitude are allowed and the stability properties of the perturbed equilibria are characteristic of the geometry of the original surface.

In global equilibrium calculations, altering the pressure may well alter the geometry of the magnetic surfaces. This in turn will affect the ballooning stability properties. In this work, we only investigate the role of profile variations; however, it is possible to incorporate variations in magnetic geometry using the formulation presented by Hegna.¹³

Dimensionless quantities are used to describe the variations in pressure gradient and shear. The equilibrium variations are parameterized by (ϵ', p') . It is convenient to use the normalized quantities $(\bar{s}, \bar{\alpha})$ defined as

$$\bar{s} = -\frac{R_0}{\epsilon' (G + \epsilon' I) \oint 1/g^{\psi\psi} \bar{\epsilon}'}, \quad (30)$$

$$\bar{\alpha} = -\frac{2V'}{\epsilon'^2} \left(\frac{V'}{(G + \epsilon' I) \oint 1/g^{\psi\psi}} \right)^{1/2} p'. \quad (31)$$

These normalizations reduce to the conventional definitions used in the shifted circle model of tokamak studies.¹⁴

III. NUMERICAL IMPLEMENTATION

The equilibria used in this study are generated by VMEC.¹⁵ The VMEC representation, assuming stellarator symmetric equilibria,¹⁶ is as follows:

$$R = \sum_{n,m} R_{n,m}(\psi) \cos(m\theta_V - n\phi), \quad (32)$$

$$Z = \sum_{n,m} Z_{n,m}(\psi) \sin(m\theta_V - n\phi), \quad (33)$$

where θ_V is the VMEC poloidal angle and the summation in the VMEC convention includes the terms $n=0, N$ for $m=0$ and $n=-N, N$ for $m=1, M-1$. The VMEC equilibrium, or more precisely a selected flux surface in the VMEC equilibrium, is occasionally referred to in this article as the “original” equilibrium, upon which variations in the profiles are performed.

The Boozer coordinate information is expressed

$$R = \sum_{n,m} R_{n,m}^B \cos(m\theta - n\zeta), \quad (34)$$

$$\phi = \zeta + \sum_{n,m} \phi_{n,m}^B \sin(m\theta - n\zeta), \quad (35)$$

$$Z = \sum_{n,m} Z_{n,m}^B \sin(m\theta - n\zeta), \quad (36)$$

where similarly the summation includes the terms $n=0, N_B$ for $m=0$ and $n=-N_B, N_B$ for $m=1, M_B-1$.

The identities Eqs. (4), (5), (6) are useful for examining the numerical accuracy of both the original equilibrium and the transformation to Boozer coordinates.

To implement the method numerically it is necessary to compute the term D appearing in Eq. (18). It is most convenient to solve separately for the coefficients of ϵ' and p' , as later these will be varied separately. By noting that $1/g^{\psi\psi}$ and $\lambda/g^{\psi\psi}$ are even functions for stellarator symmetric configurations,¹⁶ D may be written

$$D = \epsilon'^{(1)'} \sum' D_{\epsilon' mn} \sin(m\theta - n\zeta) - p'^{(1)'} \sum' D_{p' mn} \sin(m\theta - n\zeta), \quad (37)$$

where the summation excludes $(n, m) = (0, 0)$ and

$$D_{\epsilon' mn} = \frac{(1/g^{\psi\psi})_{mn}}{(\epsilon' m - n)(1/g^{\psi\psi})_{0,0}}, \quad (38)$$

$$D_{p' mn} = \frac{V'(G + \epsilon' I)}{(\epsilon' m - n)(1/g^{\psi\psi})_{0,0}} \times [(1/g^{\psi\psi})_{0,0}(\lambda/g^{\psi\psi})_{mn} - (\lambda/g^{\psi\psi})_{0,0}(1/g^{\psi\psi})_{m,n}]. \quad (39)$$

All quantities in this expression are provided by the original equilibrium represented in Boozer coordinates. After the $D_{\epsilon' mn}, D_{p' mn}$ have been evaluated, no further equilibrium computations or equilibrium variation computations are required. Arbitrary variations in p', ϵ' may be made, and the perturbed ballooning equation directly solved.

A numerical code, STESA (STellarator $s - \alpha$), that solves for D and calculates the ballooning eigenvalues has been developed. The numerical procedure used to solve the ballooning equation is to represent the eigenvector on a discrete grid along the chosen field line, with derivatives evaluated on the half-grid. This reduces the problem to that of finding the eigenvalue and corresponding eigenvector of a tridiagonal matrix. To this extent, the numerical procedure is equivalent to that used by COBRA,¹⁷ with the exception that COBRA also uses Richardson's extrapolation and variational refinement to improve the eigenvalue estimate and thus is more efficient numerically. The computational intensive component of the calculation is the determination of the coefficients of the ballooning equation. This takes the form of a Fourier summation of the metric elements. To implement the method of profile variations, the only additional computation required at this point is the determination of L , which, given the original equilibrium and p', ϵ' , is a Fourier summation of the $D_{\epsilon' mn}, D_{p' mn}$ harmonics and does not add significantly to the calculation.

The ballooning eigenvalue solver used in this work has been bench-marked against COBRAVMEC,¹⁸ an extension of COBRA written in VMEC coordinates. In benchmarking the eigenvalue solver in STESA against COBRAVMEC, it was necessary to increase both the Fourier resolution of both the VMEC equilibrium and the transformation to Boozer coordinates to obtain good agreement with the ballooning profiles: particularly so at high pressure. The radial ballooning profile for all configurations considered in this article have been verified against COBRAVMEC with good agreement and will be shown in later sections.

IV. AXISYMMETRIC CASE

To understand the properties of stability boundaries in stellarators, it is useful to consider first a simpler case: a large aspect ratio, circular cross-section tokamak.^{14,19} This serves both to illuminate some of the features we may expect

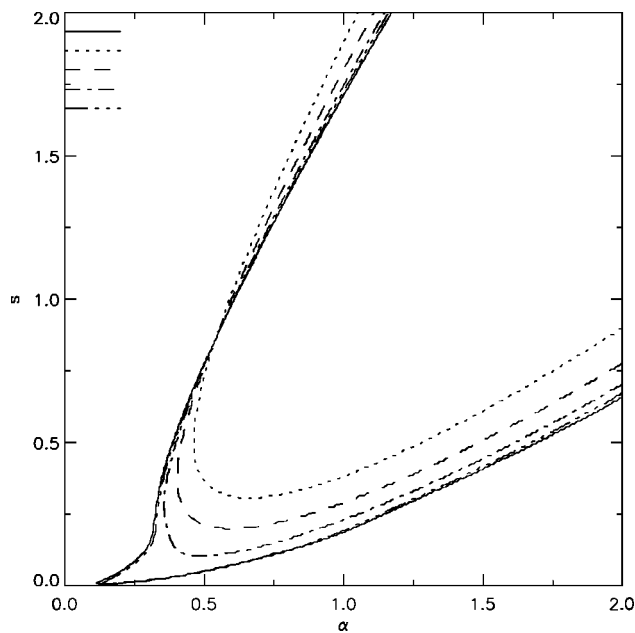


FIG. 1. $(\bar{s}, \bar{\alpha})$ diagrams for large aspect ratio, circular cross-section tokamak. As the aspect ratio A increases (dotted $A=10$, dashed $A=20$, dashed-dotted $A=50$, dashed-dotted-dotted $A=100$) the stability boundary converges to the infinite aspect ratio model (solid) boundary.

in toroidal configurations, and enables us to see later the nonaxisymmetric effect on stability boundaries. Also, it serves as a useful benchmark for the numerical results.

A series of circular cross-section axisymmetric equilibria, with increasing aspect ratio is constructed. Each configuration is given a broad pressure profile to resemble the sharp-boundary model, but this detail is somewhat irrelevant as the it is only the pressure gradient p' at the magnetic surface of interest that directly affects the ballooning stability (though the pressure profile and β may alter the geometry and thus indirectly affect the ballooning stability), and p' itself is varied to construct the stability curves. For each case, the $(\bar{s}, \bar{\alpha})$ marginal stability diagram is constructed and as shown in Fig. 1 there is good convergence to the model (infinite aspect ratio) case. In fact, it is difficult to distinguish the $A=100$ stability curve with $A=\infty$ curve. The numerical resolution of VMEC is 299 surfaces (with the 240th surface selected), $M=10, N=0$, the resolution the Boozer transformation is $M_B=40, N_B=0$. Numerical infinity η_∞ for the ballooning calculation is set to $\pm 40 \times 2\pi$ poloidal, with 50 grid points per 2π for the finite difference calculation of the ballooning eigenvalue. The large “numerical-infinity” is required to correctly describe the eigenmodes near $(\bar{s}, \bar{\alpha})=(0,0)$, as the modes become quite extended near this point.

Ballooning modes are pressure driven instabilities, and the driving force is the relative direction of the curvature and the pressure gradient. The pressure gradient is negative in all these cases, so there is potentially an instability when the curvature is negative. The effect of local shear is to contribute a stabilizing effect through field line bending. The local shear is related to the pressure gradient through the Pfirsch-Schlüter modulation as described by the term proportional to $p^{(1)'} in Eq. (18), and as the pressure increases the pressure$

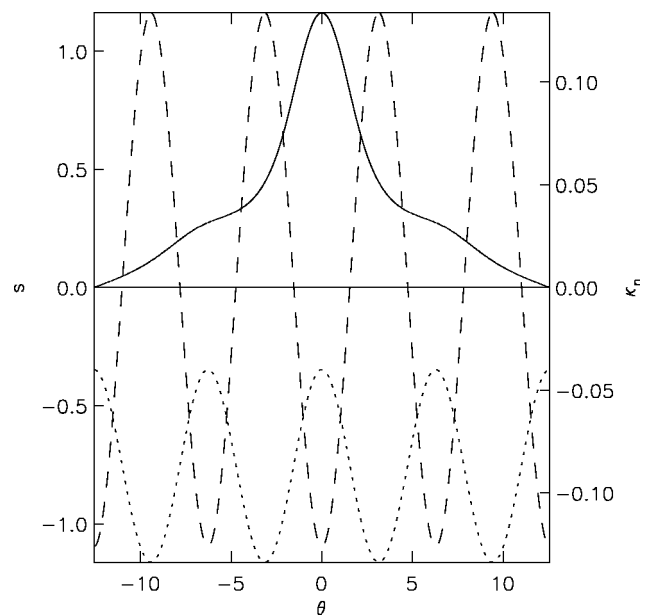


FIG. 2. Eigenvector (solid), local shear (dotted), and normal curvature (dashed) for the equilibrium in the first stable region $(\bar{s}, \bar{\alpha})=(0.50, 0.25)$.

induced modulation of the local shear increases. When regions of small local shear $|s|$ coincide with regions of negative curvature, a ballooning instability can occur.

In Figs. 2, 3, 4, eigenvectors, the normal curvature and local shear are shown for the aspect ratio $A=50$ configuration in the first stable region $(\bar{s}, \bar{\alpha})=(0.50, 0.25)$, the unstable region $(\bar{s}, \bar{\alpha})=(0.25, 0.50)$ and the second stable region $(\bar{s}, \bar{\alpha})=(0.75, 0.00)$ of Fig. 1. In the first stable region, $|s|$ is sufficiently large in the negative curvature region to stabilize the modes. In the unstable region, $|s|$ goes to zero in the negative curvature region and a localized mode can exist. In the second stable region, $|s|$ is again sufficiently large in

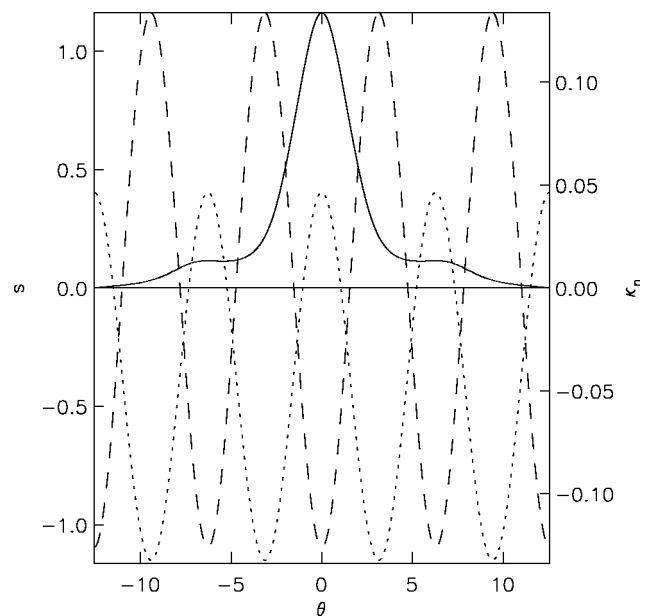


FIG. 3. Eigenvector (solid), local shear (dotted), and normal curvature (dashed) for the equilibrium in the unstable region $(\bar{s}, \bar{\alpha})=(0.25, 0.50)$.

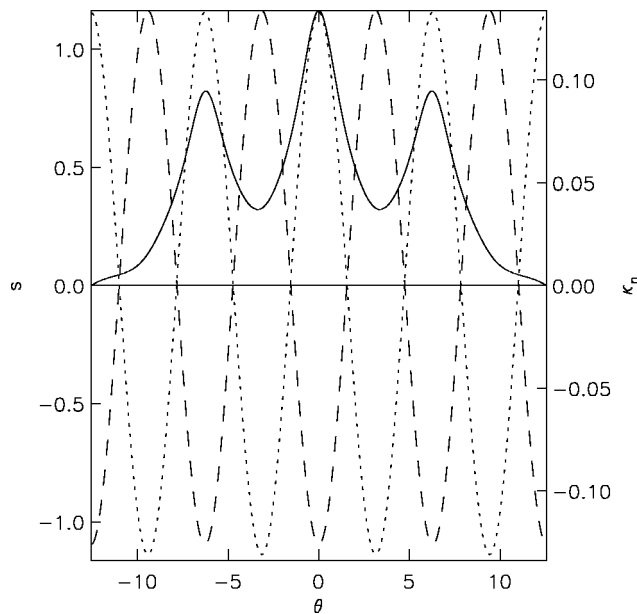


FIG. 4. Eigenvector (solid), local shear (dotted), and normal curvature (dashed) for the equilibrium in the second stable region $(\bar{x}, \bar{\alpha}) = (0.00, 0.75)$.

negative curvature region to stabilize (broaden) the eigenmode. Note that for the purposes of illustration, “numerical-infinity” is chosen $\pm 2 \times 2\pi$ for these eigenvector diagrams.

V. QUASIAxisymmetric CASE

We consider a quasiaxisymmetric stellarator configuration considered in the design of the National Compact Stellarator eXperiment (NCSX).^{20,21,22} The ballooning instability mechanisms in a quasi-axisymmetric stellarator have been studied in Refs. 23, 24, 25. The fixed-boundary design li383 is studied. Cross sections in Boozer coordinates of li383 at low pressure and high pressure are shown in Figs. 5 and 6. The pressure and rotational-transform profiles for various pressures are shown in Fig. 7. For the high pressure case, there is a noticeable deformation of the coordinates, which indicates a change in the geometry of the inner surfaces. As the method of constructing marginal stability diagrams considered in this article is geometry dependent, we may expect that the marginal stability diagrams will change as the pressure (and thus the magnetic coordinate geometry) is increased. Note that these configurations, particularly the high-pressure configurations, are not intended to be realized in the experimental operation of NCSX. They may be considered as suitable example equilibria intended for study.

A comparison of the ballooning profiles ($\lambda \sim -\omega^2$) from STESA and COBRAVMEC for various pressures are shown in Figs. 8, 9, 10. The ballooning profiles show that li383 is marginally unstable to ballooning modes for $\beta = 4.20\%$, and is unstable over a large region of the minor radius $0.3 < \psi < 0.95$ at $\beta = 11.93\%$; however, as the pressure is further increased the surfaces $0.35 < \psi < 0.6$ become stable.

The STESA and COBRAVMEC profiles show good agreement in the location of marginal stability. Note that there are differences in the normalization of the eigenvalue

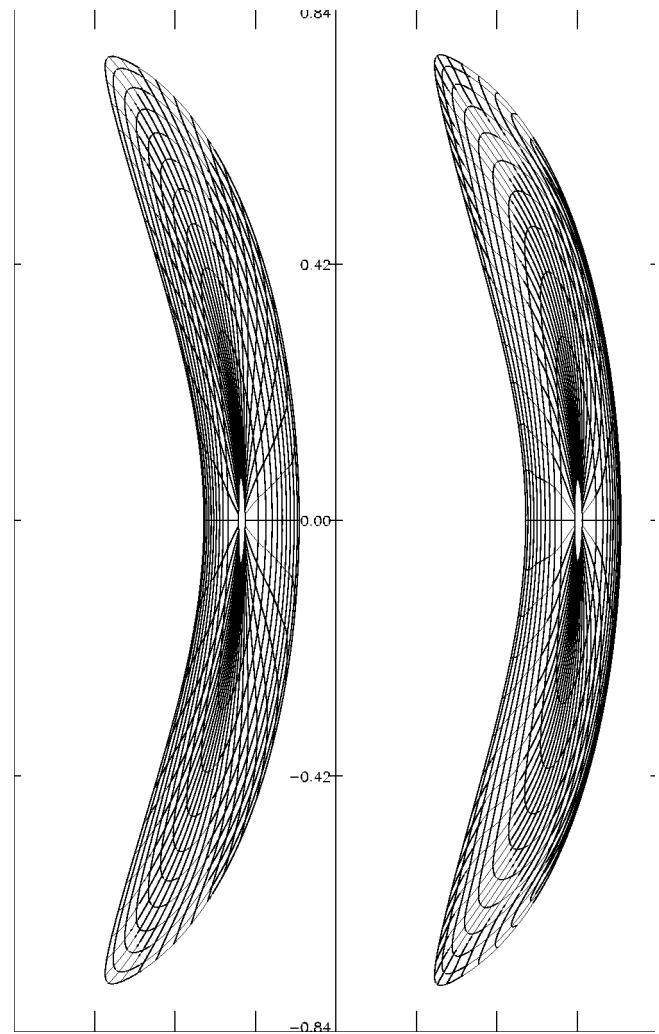


FIG. 5. Cross section of Boozer coordinates of li383 at $\beta = 0.32\%$ (left) and $\beta = 16.43\%$ (right) for li383 on the $\zeta = 0$ plane.

between these codes. For these ballooning profiles, the eigenvalue depends upon field line label α and ballooning angle η_k . Unless stated otherwise, we use the choice $\alpha = 0, \eta_k = 0$ in these calculations. For this study, M, N

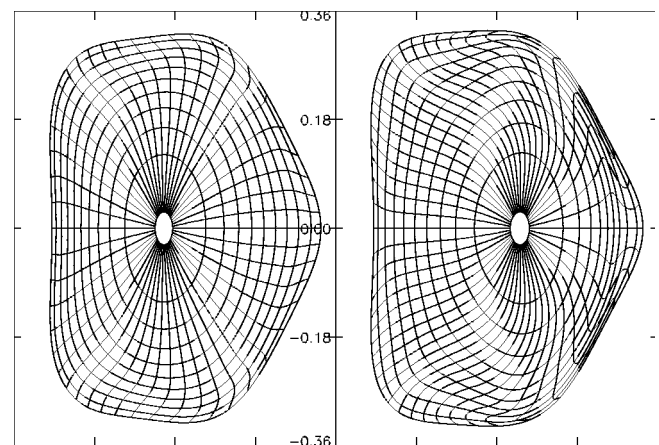


FIG. 6. Cross section of Boozer coordinates of li383 at $\beta = 0.32\%$ (left) and $\beta = 16.43\%$ (right) for li383 on the $\zeta = 2\pi/6$ plane.

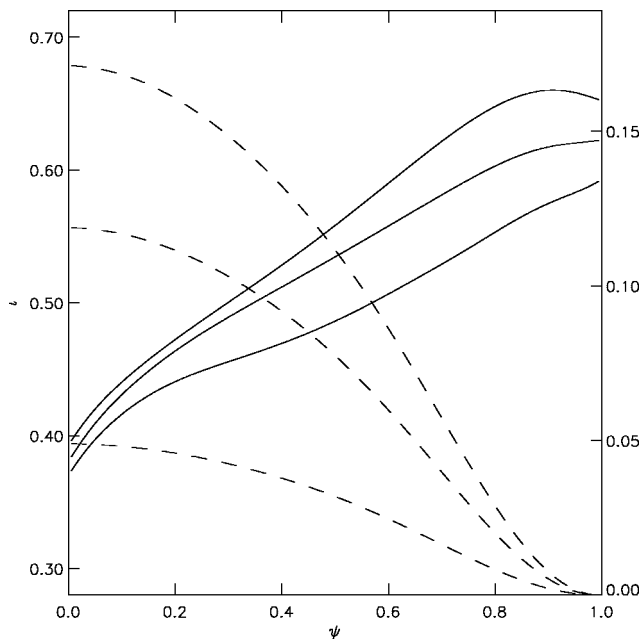


FIG. 7. Rotational-transform (solid) and pressure (dashed) profiles for li383 at $\beta = 4.53\%$, 11.2416% , 16.43% .

$=18,10$ in Eqs. (32), (33) which results in 368 Fourier harmonics, and $M_B = 8M, N_B = 8N$ in Eqs. (34), (35), (36) which results in 22817 Fourier modes to describe the equilibrium in Boozer coordinates. The radial resolution used was $ns = 100$. This resolution was deemed sufficient by the agreement between the STESA ballooning solver and COBRAVMEC.

Marginal stability diagrams for li383 at $\beta = 4.20\%$, 11.93% , and 16.43% , on surfaces $\psi = 0.30, 0.50$ and $\psi = 0.80$ are shown in Figs. 11, 12, 13. In each of these diagrams, the location of the original equilibrium is also

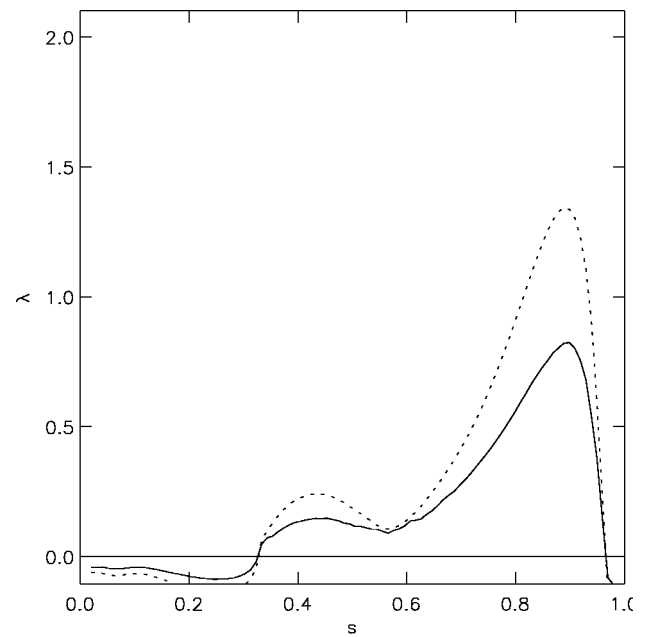


FIG. 9. Ballooning radial profile from STESA (solid) and COBRAVMEC (dotted) for li383 at $\beta = 11.93\%$.

shown. The field line label $\alpha = 0$ and the ballooning angle $\eta_k = 0$. Figure 11 suggests there will be a second stable region for the $\psi = 0.5$ and $\psi = 0.8$ surfaces, but not for the $\psi = 0.3$ surface, in apparent agreement with the ballooning eigenvalue profiles. For this case, the location of the original equilibrium for the $\psi = 0.5$ and $\psi = 0.8$ surfaces in $(\bar{s}, \bar{\alpha})$ space coincide. As the pressure is increased to $\beta = 11.93\%$, all the original surfaces are in the unstable region. The stability boundaries have changed slightly, with the stability boundary for the $\psi = 0.3$ surface now showing the existence of second-stability. For the $\beta = 16.43\%$ case, the original ψ

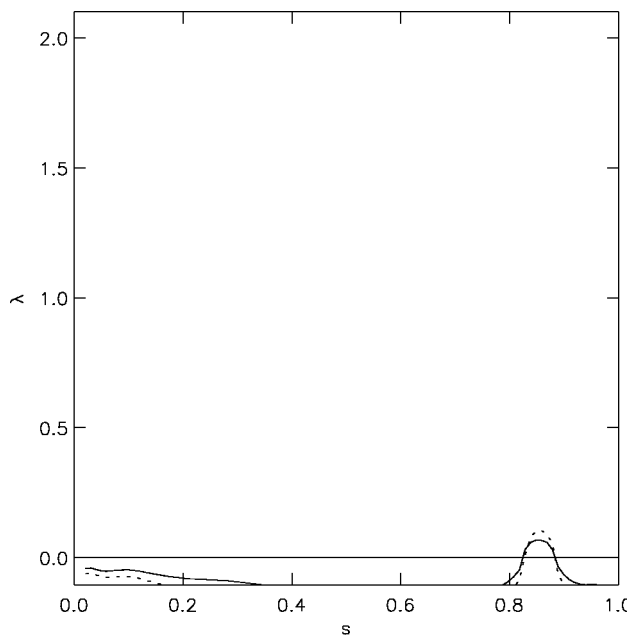


FIG. 8. Ballooning radial profile from STESA (solid) and COBRAVMEC (dotted) for li383 at $\beta = 4.20\%$.

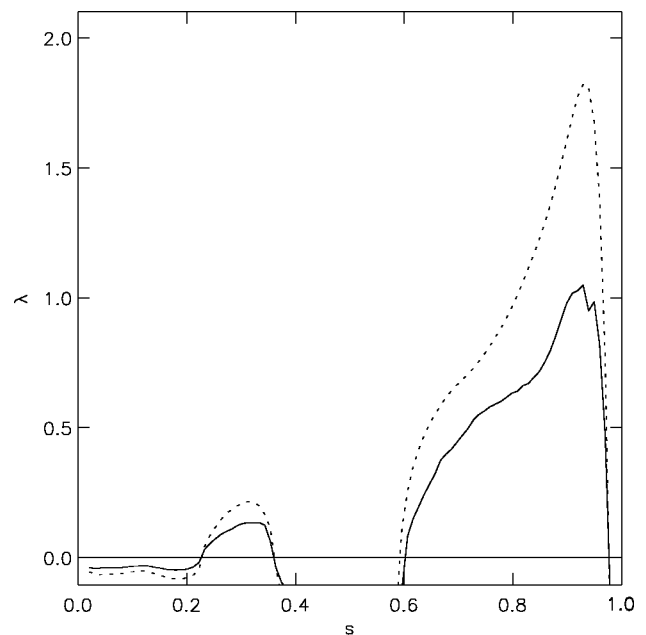


FIG. 10. Ballooning radial profile from STESA (solid) and COBRAVMEC (dotted) for li383 at $\beta = 16.43\%$.

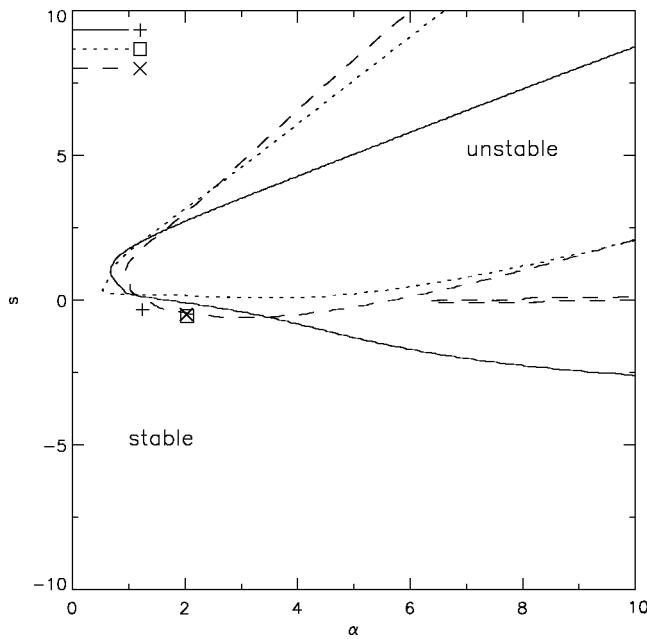


FIG. 11. (s, α) diagrams for the $\psi_b=0.3$ (solid), 0.5 (dotted), and 0.8 (dashed) surfaces in NCSX li383 at $\beta=4.20\%$. The position of the initial equilibrium (for each surface) is also shown.

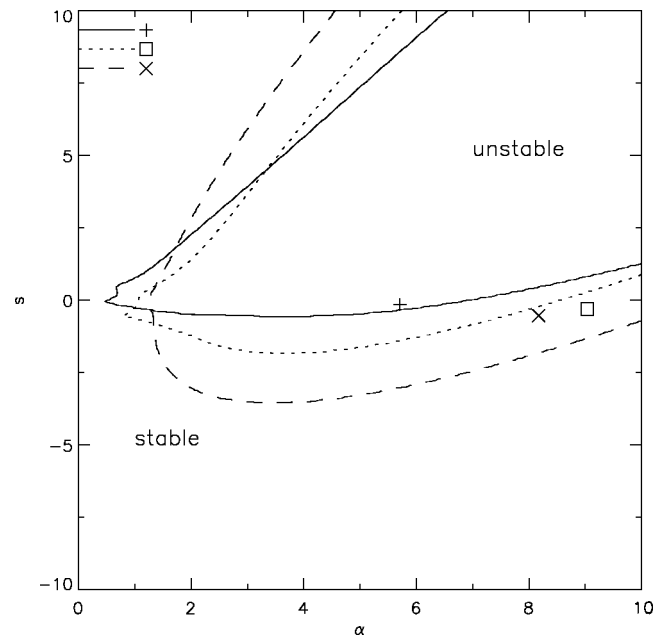


FIG. 13. (s, α) diagrams for the $\psi_b=0.3$ (solid), 0.5 (dotted), and 0.8 (dashed) surfaces in NCSX li383 at $\beta=16.43\%$. The position of the initial equilibrium (for each surface) is also shown.

$=0.5$ surfaces is now in the second stable region. The stability boundary for each surface suggests the existence of second-stability, provided that dramatic geometric variations do not occur.

It will be interesting to examine higher pressure equilibria to examine whether the suggested second-stability indeed exists on all surfaces simultaneously. An attempt to construct higher pressure equilibria was performed, but with the high numerical resolution parameters used here some difficulty

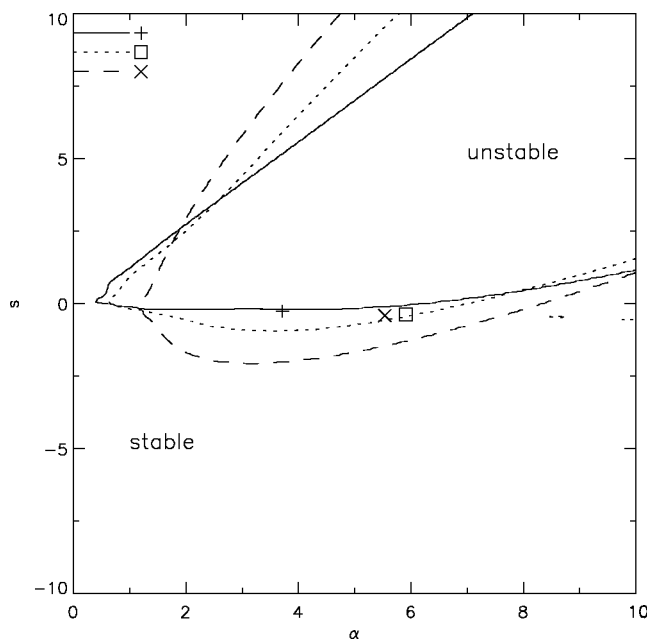


FIG. 12. (s, α) diagrams for the $\psi_b=0.3$ (solid), 0.5 (dotted), and 0.8 (dashed) surfaces in NCSX li383 at $\beta=11.93\%$. The position of the initial equilibrium (for each surface) is also shown.

was encountered with VMEC convergence and the accuracy of the transformation to Boozer coordinates at high pressure. To enable marginal stability diagrams and to determine if the region of second-stability extends over the entire plasma for stellarator configurations with very high β ($\beta > 20\%$), it may be necessary to follow the example of COBRAVMEC (Ref. 18) and develop the theory of profile variations in VMEC coordinates, thus alleviating some of the convergence problems. Nevertheless, through the use of the profile variation method, this work suggests that quasisymmetric stellarators may exist with ballooning stable profiles at high β .

It is interesting to compare the behavior of the eigenvectors, the normal curvature and local shear to that of the large aspect-ratio circular-cross section tokamak. In Figs. 14, 15, 16 are shown the behavior of the eigenvectors, normal curvature, and shear along the field line in the first stable, unstable and second stable regions for the $\beta=11.93\%$ case. The behavior of the curvature and local shear is quite complicated in the stellarator case and for clarity only the region near the "origin" $\eta_k=0$ is shown. The value $\eta_k=0$ is used throughout this study. In the three cases shown, this is where the eigenmode peaks and thus it is reasonable to expect that this is where the eigenmode is most sensitive to variations in the local shear.

At $\eta_k=0$, the curvature is negative so there is the potential for a localized ballooning mode to exist. In the first stable region, the local shear is negative, apparently with sufficient magnitude to prevent a localized mode from forming. The ballooning mode for this case is comparatively broad. As p' is increased, the local shear increases and passes through zero at $\eta_k=0$ and the ballooning mode now becomes localized and unstable. In the second stable region, as the pressure is further increased the local shear increases and now has sufficient magnitude to stabilize and broaden

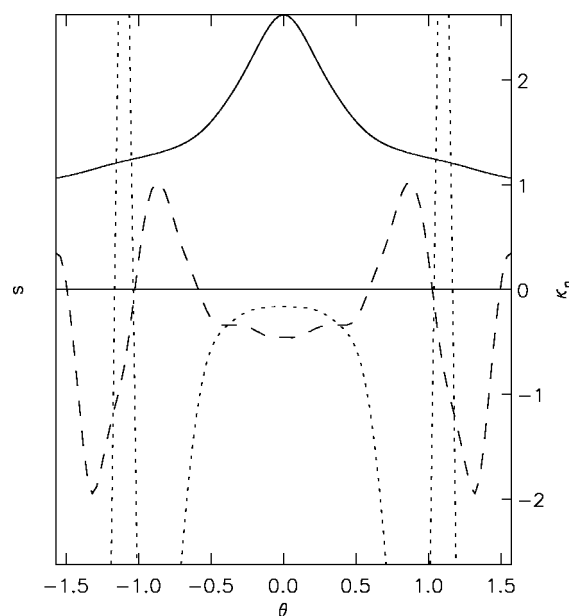


FIG. 14. Eigenvector (solid), normal curvature (dashed) and shear (dotted) for $\beta=11.93\%$, $\psi=0.80$, $(\bar{s}, \bar{\alpha})=(2.5, 1.0)$.

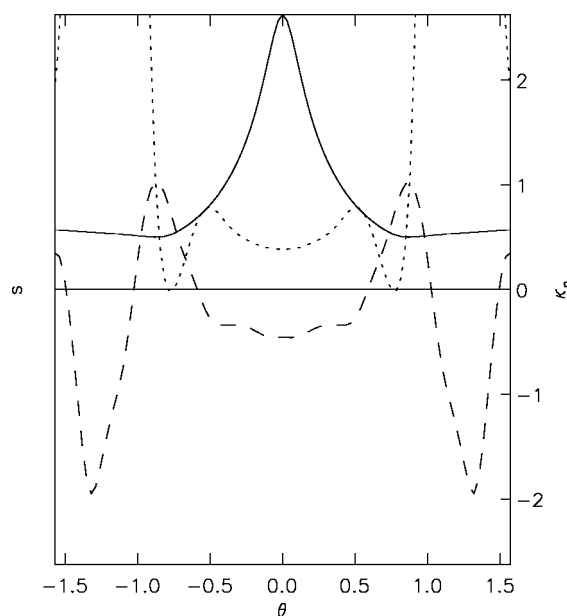


FIG. 16. Eigenvector (solid), normal curvature (dashed), and shear (dotted) for $\beta=11.93\%$, $\psi=0.80$, $(\bar{s}, \bar{\alpha})=(-2.5, 5.0)$.

the mode. The behavior is thus similar to that observed in the tokamak case.

Note that though the simple picture that ballooning instability occurs when small local shear and bad curvature coincide is consistent with both the tokamak and quasisymmetric stellarator case presented here, an exhaustive investigation and confirmation of this has not yet been performed. The structure of both the curvature and local shear is quite complicated in the stellarator case.

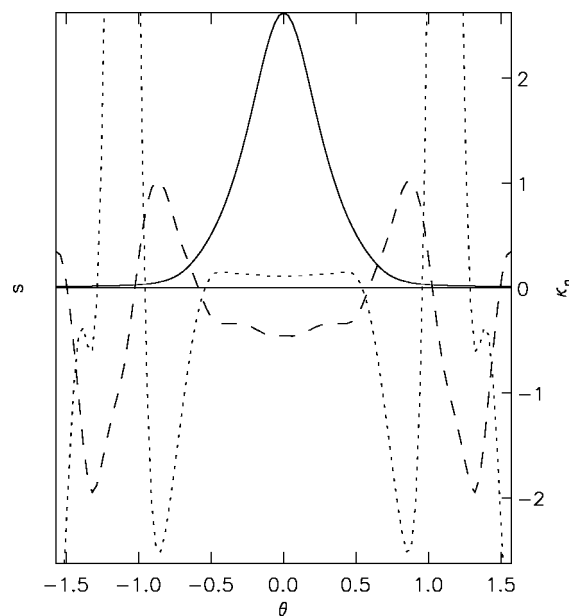


FIG. 15. Eigenvector (solid), normal curvature (dashed) and shear (dotted) for $\beta=11.93\%$, $\psi=0.80$, $(\bar{s}, \bar{\alpha})=(0.0, 3.0)$.

VI. VARIATION OF FIELD LINE LABEL

A unique feature of three-dimensional geometry is that the ballooning eigenvalue λ will depend not only on the flux surface label ψ and the ballooning angle η_k , but also on the magnetic field line label α : $\lambda = \lambda(\psi, \alpha, \eta_k)$. This is not case in axisymmetric systems where the ballooning eigenvalue is a function of the surface and ballooning angle only: $\lambda = \lambda(\psi, \eta_k)$. This dependency on magnetic field line label adds complexity to solving the full WKB problem;²⁶ however, there are examples of three-dimensional systems showing that global ballooning spectrum properties can in some cases be accurately predicted from the WKB-ballooning theory.²⁷⁻²⁹

In Fig. 17, the dependence of the ballooning eigenvalue on magnetic field line ($\alpha = \theta - \iota \zeta$) is shown for the $\beta = 16.44\%$ case on the magnetic surfaces $\psi=0.30, 0.50$, and 0.80 . Note that for the $\psi=0.30, 0.80$ surfaces, the ballooning eigenvalue is near the maximum at $\alpha=0$; however, for the $\psi=0.50$ surface, the eigenvalue is near a minimum. This suggests that the stability boundaries shown in the previous section will likely be altered as the field line label is allowed to vary. Additionally, it is interesting to note that on the same magnetic surface, for all three magnetic surfaces, there is a mixture of field lines with negative and positive ballooning eigenvalues.

In Figs. 18, 19, 20, the marginal stability boundaries are plotted for the $\beta = 16.44\%$ case with $\alpha = 1.04720$. While the structure of these diagrams is qualitatively similar to the $\alpha = 0$ case, there are important quantitative differences. The diagram for the $\psi=0.8$ surface suggests that the second stable region is fractured.

The dependence of the eigenvalue on η_k has not been examined here.

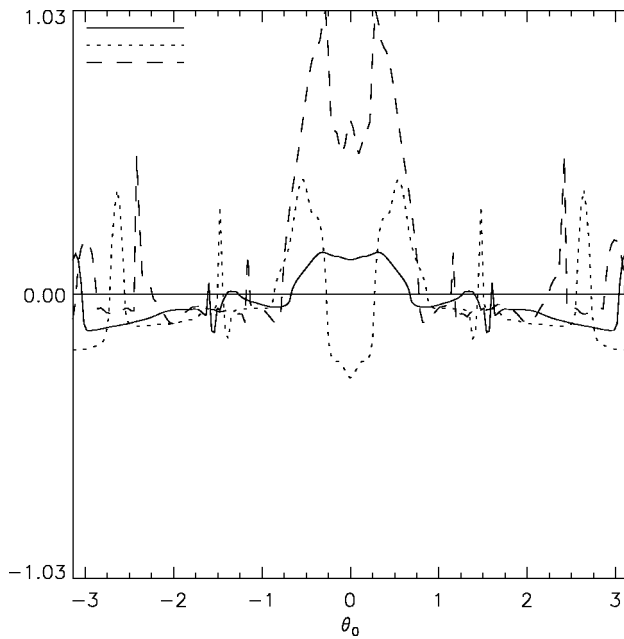


FIG. 17. Dependence of ballooning eigenvalue on field line label α for the $\beta=16.43\%$ case for surfaces $\psi=0.30$ (solid), 0.50 (dotted), and 0.80 (dashed).

VII. DISCUSSION

In this work, a study of the ideal MHD ballooning stability properties of a quasisymmetric stellarator is presented. In particular, the marginal stability properties as functions of plasma profiles have been examined using the procedure introduced by Greene and Chance³ and generalized to three-dimensional systems by Hegna and Nakajima.¹¹ This technique allows one to manipulate the plasma profiles

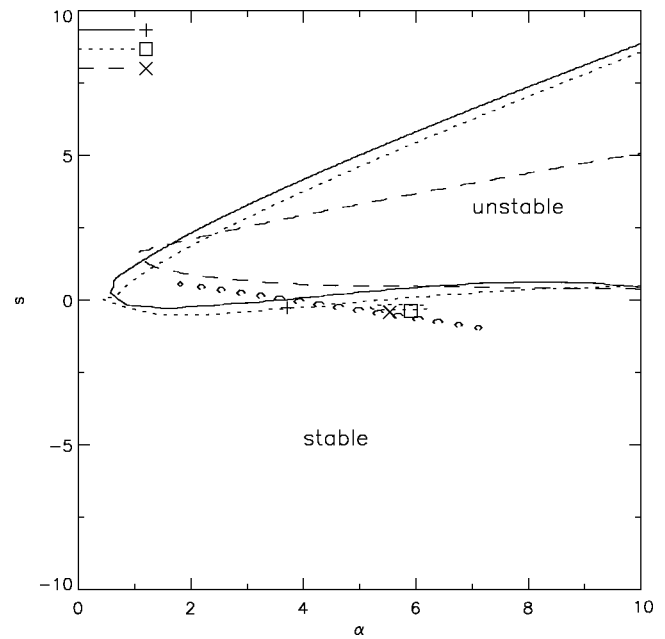


FIG. 19. (s, α) diagrams for the $\psi_b=0.3$ (solid), 0.5 (dotted), and 0.8 (dashed) surfaces in NCSX li383 at $\beta=11.93\%$ with the field line label $\alpha=1.04720$. The position of the initial equilibrium (for each surface) is also shown.

in the vicinity of a particular magnetic surface, keeping the magnetic geometry fixed, while ensuring that the MHD equilibrium condition is satisfied. By using this technique, a generalization of (s, α) curves used prominently in tokamak ballooning calculations can be constructed for general three-dimensional equilibria.

The marginal stability diagrams for the quasisymmetric stellarator case studied in this article have a number of

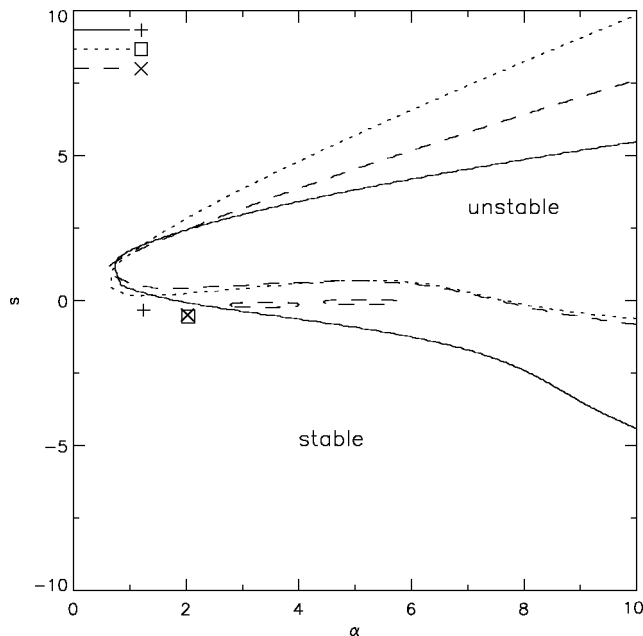


FIG. 18. (s, α) diagrams for the $\psi_b=0.3$ (solid), 0.5 (dotted), and 0.8 (dashed) surfaces in NCSX li383 at $\beta=4.20\%$ with field line label $\alpha=1.04720$. The position of the initial equilibrium (for each surface) is also shown.

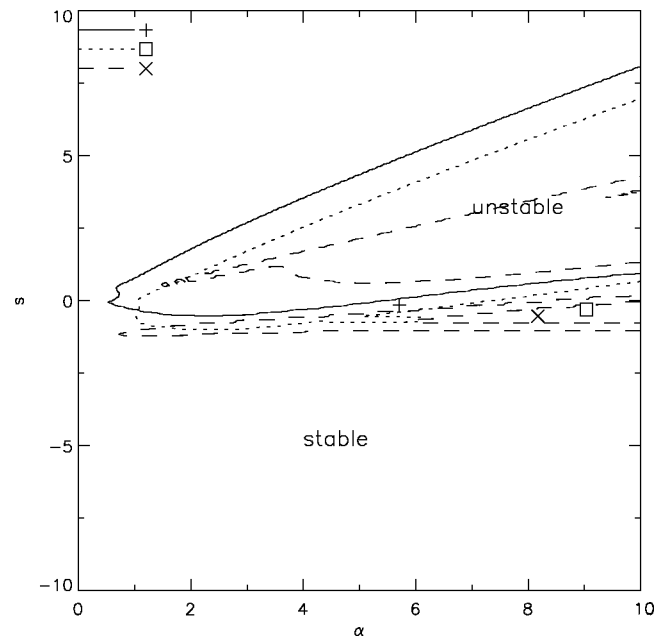


FIG. 20. (s, α) diagrams for the $\psi_b=0.3$ (solid), 0.5 (dotted), and 0.8 (dashed) surfaces in NCSX li383 at $\beta=16.43\%$ with field line label $\alpha=1.04720$. The position of the initial equilibrium (for each surface) is also shown.

similarities to the marginal stability diagrams of axisymmetric tokamaks; however, there are some important differences. Both configurations show a stability boundary in the “tokamak-like” shear ($\bar{s} \sim -d\psi/d\psi > 0$) region where the critical pressure gradient for instability rises (nearly) monotonically with average magnetic shear. This can be seen by comparing the $\bar{s} > 0$ regions of Fig. 1 and Figs. 11, 12, 13. In this “strong-shear” limit, the ballooning eigenmode is localized to a narrow range along the field line where the curvature is unfavorable. In this region of profile space, the quasisymmetric stellarator and the tokamak have similar ballooning properties.

Where the quasisymmetric stellarator and axisymmetric tokamak differ is when \bar{s} becomes small. For tokamaks, there are no unstable ballooning modes for zero or “stellarator-like” magnetic shear ($\bar{s} \leq 0$); however, for stellarators, unstable ballooning modes can exist in the $\bar{s} \leq 0$ region of parameter space. The underlying reason for this is the three-dimensional nature of the important geometric objects (local shear and curvature) that govern the marginal stability properties. Various workers^{30–33} have studied the local magnetic shear in nonaxisymmetric configurations. In this region of parameter space, the variation of the local shear within the magnetic surface can dominate the averaged shear. Since the harmonic structure of the local shear has incommensurate helicity with the prominent toroidal curvature, the ballooning eigenmode can localize to particular region along the field line with bad curvature.^{4,34} Cuthbert and co-workers demonstrated that this mechanism can produce unstable eigenmodes even in the limit of zero averaged shear.^{35,36}

Associated with this behavior is a sensitivity of the ballooning mode eigenvalue to the magnetic field line label. When the averaged magnetic shear becomes sufficiently small or negative, ballooning modes can be excited in quasisymmetric stellarators.

Previous work suggested that due to the three-dimensional nature of stellarators, the geometry of nonaxisymmetric systems would provide sufficient freedom for ballooning modes to find a region in which they may localize; thus deteriorate, and even eliminate, the onset of second-stability.^{4,34} While this qualitative trend is seen in the calculations presented here, quantitative calculations are needed to address the second-stability question properly. Having performed such calculations, the results indicate that there are quasisymmetric stellarators that possess regions of second-stability.

This work suggests that there may be ways to further optimize the stellarator to take advantage of second-stability. Perhaps through further shaping and/or profile optimization, a stable path through configuration space may be discovered and exploited. It will be interesting to examine the quasi-helical case at high β and to construct marginal stability diagrams for QPS.⁵

We note that the method presented enables the stability of equilibria in the neighborhood of a given equilibria to be determined with a minimum of computational effort. Thus, there is a possibility that this method will be of benefit in stellarator optimization routines.^{37,21,38} At each surface, the

pressure gradient may be altered to optimize stability, and the pressure profile itself be determined from the pressure gradient profile. A local method of optimization can become stuck in local minima. By incorporating the method of profile variations, the optimizer may be able to determine that across a small region of previously impassable instability lies a region of stability.

For stellarator geometry, the ballooning eigenvalue generally depends on all three coordinates (ψ, α, η_k). Consequently, the isosurfaces of unstable eigenvalues may have spherical topology in this space, in addition to the topological toroidal surfaces that axisymmetric configurations possess. This may lead to the global modes constructed from ray tracing being highly localized. Such highly localized modes may be stabilized by nonideal effects, and thus not be the deciding factor in determining pressure limits in stellarators.

ACKNOWLEDGMENTS

We thank Tony Cooper and Raul Sanchez for discussions on solving the ballooning equation, Roberto Torasso and Andrew Ware for discussions on ballooning stability in stellarator configurations, and Neil Pomphrey for discussions on the text.

This work was supported in part by U.S. Department of Energy Contract No. DE-AC02-76CH03073.

- ¹S. Sakakibara, H. Yamada, K. Y. Watanabe *et al.*, Nucl. Fusion **41**, 1177 (2001).
- ²A. Weller, M. Anton, J. Geiger *et al.*, Phys. Plasmas **8**, 931 (2001).
- ³J. M. Greene and M. S. Chance, Nucl. Fusion **21**, 453 (1981).
- ⁴C. C. Hegna and S. R. Hudson, Phys. Rev. Lett. **87**, 035001 (2001).
- ⁵A. S. Ware, S. P. Hirshman, D. A. Spong *et al.*, Phys. Rev. Lett. **89**, 125003 (2002).
- ⁶L. M. Kovrizhnykh and S. V. Shchepetov, Sov. J. Plasma Phys. **7**, 229 (1981).
- ⁷J. H. Harris, M. Murakami, B. A. Carreras *et al.*, Phys. Rev. Lett. **63**, 1249 (1989).
- ⁸J. H. Harris, E. Anabitarte, G. L. Bell *et al.*, Phys. Fluids **B 2**, 1353 (1990).
- ⁹B. A. Carreras, N. Dominguez, V. E. Lynch *et al.*, Fusion Technol. **23**, 71 (1993).
- ¹⁰T. Matsumoto, Y. Nakamura, and M. Wakatani, J. Phys. Soc. Jpn. **62**, 3904 (1993).
- ¹¹C. C. Hegna and N. Nakajima, Phys. Plasmas **5**, 1336 (1998).
- ¹²A. H. Boozer, Phys. Fluids **25**, 520 (1982).
- ¹³C. C. Hegna, Phys. Plasmas **7**, 3921 (2000).
- ¹⁴J. W. Connor, R. J. Hastie, and J. B. Taylor, Phys. Rev. Lett. **40**, 396 (1978).
- ¹⁵S. P. Hirshman and J. C. Whitson, Phys. Fluids **26**, 3553 (1983).
- ¹⁶R. L. Dewar and S. R. Hudson, Physica D **112**, 275 (1997).
- ¹⁷R. Sanchez, S. P. Hirshman, J. C. Whitson, and A. S. Ware, J. Comput. Phys. **161**, 576 (2000).
- ¹⁸R. Sanchez, S. P. Hirshman, and H. V. Wong, Comput. Phys. Commun. **135**, 82 (2001).
- ¹⁹J. P. Friedberg, *Ideal Magnetohydrodynamics* (Plenum, New York, 1987).
- ²⁰A. H. Reiman, G. Fu, S. Hirshman *et al.*, Plasma Phys. Controlled Fusion **41**, B273 (1999).
- ²¹G. H. Neilson, A. H. Reiman, M. C. Zarnstorff *et al.*, Phys. Plasmas **7**, 1911 (2000).
- ²²M. C. Zarnstorff, L. A. Berry, A. Brooks *et al.*, Plasma Phys. Controlled Fusion **43**, A237 (2001).
- ²³W. A. Cooper, Phys. Plasmas **7**, 2546 (2000).
- ²⁴W. A. Cooper, S. Okamura, and K. Yamazaki, Plasma Phys. Controlled Fusion **43**, 839 (2001).
- ²⁵M. H. Redi, J. L. Johnson, S. Klasky *et al.*, Phys. Plasmas **9**, 1990 (2002).
- ²⁶R. L. Dewar and A. H. Glasser, Phys. Fluids **26**, 3038 (1983).
- ²⁷W. M. Nevins and L. D. Pearlstein, Phys. Fluids **31**, 1988 (1988).

- ²⁸W. A. Cooper, D. B. Singleton, and R. L. Dewar, Phys. Plasmas **3**, 275 (1996).
- ²⁹O. Yamagishi, Y. Nakamura, K. Kondo, and N. Nakajima, Phys. Plasmas **9**, 3429 (2002).
- ³⁰R. E. Waltz and A. H. Boozer, Phys. Fluids B **5**, 2201 (1993).
- ³¹N. Nakajima, Phys. Plasmas **3**, 4545 (1996).
- ³²W. A. Cooper, Phys. Plasmas **4**, 153 (1997).
- ³³M. Nadeem, T. Rafiq, and M. Persson, Phys. Plasmas **8**, 4375 (2001).
- ³⁴C. C. Hegna and S. R. Hudson, Phys. Plasmas **9**, 2014 (2002).
- ³⁵P. Cuthbert, J. L. V. Lewandowski, H. J. Gardner *et al.*, Phys. Plasmas **5**, 2921 (1998).
- ³⁶P. Cuthbert and R. L. Dewar, Phys. Plasmas **7**, 2302 (2000).
- ³⁷R. Sanchez, S. P. Hirshman, A. S. Ware *et al.*, Plasma Phys. Controlled Fusion **42**, 641 (2000).
- ³⁸D. A. Spong, S. P. Hirshman, L. A. Berry *et al.*, Nucl. Fusion **41**, 711 (2001).